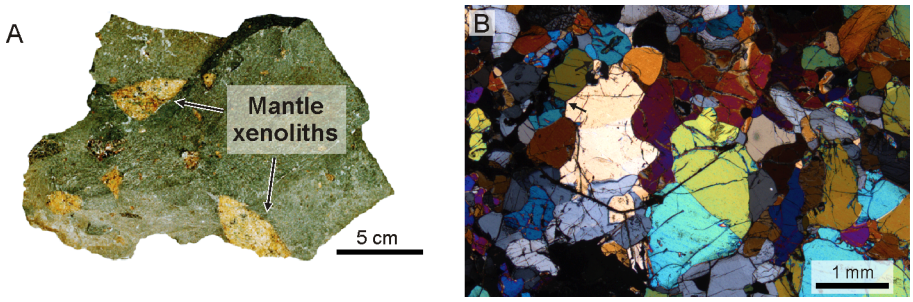

Figure DR1. SAF mantle xenoliths. A: Photograph of peridotite xenoliths within basalt matrix. B: Photomicrograph of a lherzolite xenolith (crossed polars). The xenolith is characterized by olivine porphyroclasts with planar internal subgrains and dynamically recrystallized grains along the porphyroclast boundaries. Grain shapes are dominantly lobate. Polygonal grains with 120^{o} triple junctions between olivine grains (black arrows) and the smaller (recrystallized) grains along olivine porphyroclasts margins, are also present.

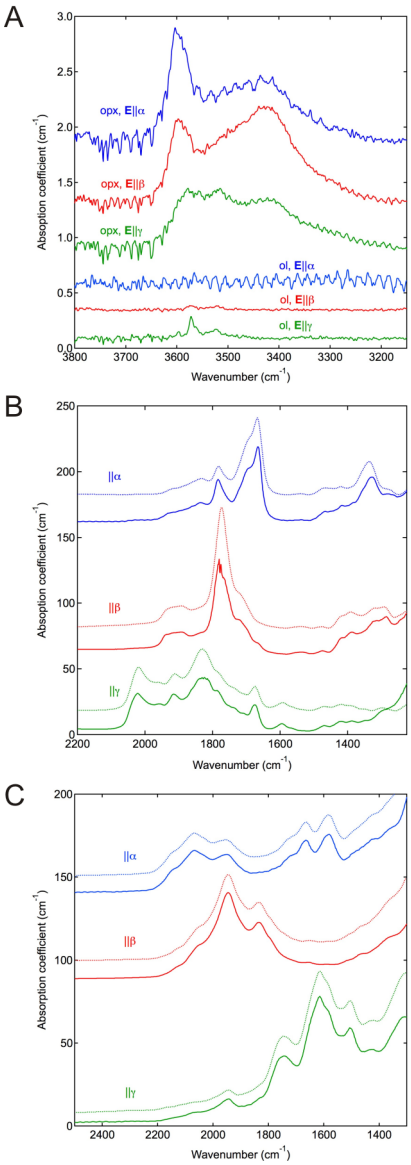

Figure DR2. FTIR spectra from olivine and orthopyroxenene. Polarized transmission FTIR spectra collected from oriented crystal sections of olivine and orthopyroxene from a single xenolith. Infrared spectra were collected using a Bruker Tensor 37 FTIR spectrometer and Hyperion 2000 microscope. Sample preparation techniques and analysis conditions followed those described in Withers et al. (2011). Polarized spectra were collected parallel to the **a**, **b**, and **c** axes of olivine and orthopyroxene crystals. We used the calibration of Withers et al. (2012) for determining the H content in olivine and Bell et al. (1995) for orthopyroxene. Spectra are normalized to the sample thickness in cm and offset for clarity. A: Olivine (ol) and orthopyroxene (opx) FTIR spectra in the OH stretching region. Spectra have been baseline corrected. Opx spectra exhibit absorption bands at 3600 and 3425 cm^{-1}, and olivine spectra show weak absorption at 3572 and 3523 cm^{-1}. Spectra are labeled with the polarization direction of the electric vector of the infrared light (E), relative to the axes of the infrared indicatrix. B: Principal spectra used for orientation for sample GRR997 (Asimow et al., 2006) (dotted curves) and for olivine from this study (solid curves) in the region from 1200 to 2200 cm^{-1}. The most strongly absorbing peaks in the E||β and E||γ spectra are clipped owing to near-complete infrared absorbance at these frequencies in a 470 µm thick crystal section. C: Principal spectra used for orientation for sample KBH-1 (Mosenfelder and Rossman, 2013) (dotted curves) and for orthopyroxene from this study (solid curves) in the region between 1300 and 2500 cm^{-1}.

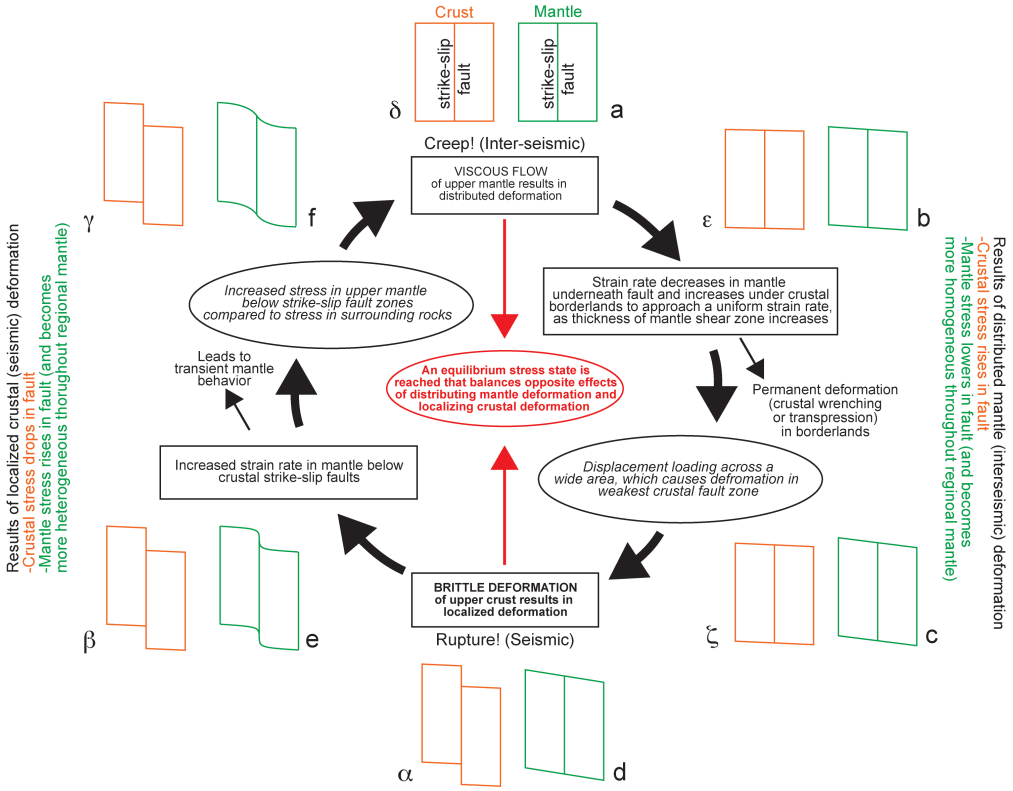

Figure DR3. Feedback loop of the Lithospheric Feedback model for western California, in which both the viscous mantle and frictional crust contribute to system behavior. We consider the deformation, both within the fault and within the borderlands, from two points of view: 1) Displacement; and 2) Stresses. During a seismic cycle, the displacement viewpoint is shown in blocks, representing horizontal slices through the upper crust and lithospheric mantle. The blocks with the Roman letters a-f describe the displacement in the mantle, while the blocks with the Greek letters α-ζ describe the displacement in the crust during a seismic cycle. Distributed flow in the mantle causes displacement loading of the crust, resulting in diffuse crustal deformation and ultimately seismic rupture on strike-slip faults. Strain localization in the crust controls the stress cycle, as lithospheric mantle rocks respond to rupture (α) by increasing strain rate and stress in the shear zone below the crustal segment of the fault. As a response to this strain rate increase, the lithospheric mantle undergoes viscous relaxation (e-f) and dissipates the localized deformation due to fault rupture.

REFERENCES

Asimow, P.D., Stein, L.C., Mosenfelder, J.L., and Rossman, G.R., 2006, Quantitative polarized FTIR analysis of trace OH in populations of randomly oriented mineral grains: American Mineralogist, v. 91, 278−284.

Bell, D.R., Ihinger, P.D., and Rossman, G.R., 1995, Quantitative analysis of trace OH in garnet and pyroxenes: American Mineralogist, v. 80, 465−474.

Mosenfelder, J.D., and Rossman, G.R., 2013, Analysis of hydrogen and fluorine in pyroxenes by SIMS and FTIR. Part I. Orthopyroxene: American Mineralogist, v. 98, 1026−1041.

Withers, A.C., Hirschmann, M.M., and Tenner, T.J., 2011, The effect of Fe on olivine H2O storage capacity: Consequences for H2O in the Martian mantle: American Mineralogist, v. 96, 1039−1053.

Withers, A.C., Bureau, H., Raepsaet, C., and Hirschmann, M.M., 2012, Calibration of infrared spectroscopy by elastic recoil detection analysis of H in synthetic olivine: Chemical Geology, v. 334, 92−98.

Table DR1. Paleopiezometry results

Sample	Corrected (3D) recrystallized grain size (μm)			Differential Stress (MPa)			Strain Rate (s^{-1})			Viscosity ($Pa{\cdot}s$)		
	Dchord	Dmax	Deq	Dchord	Dmax	Deq	Dchord	Dmax	Deq	Dchord	Dmax	Deq
CAB18-2A	711.7	644.1	477.2	9.8	10.5	13.2	$8.2{\cdot}10^{-14}$	$1.1{\cdot}10^{-13}$	$2.9{\cdot}10^{-13}$	$3.0{\cdot}10^{19}$	$2.4{\cdot}10^{19}$	$1.1{\cdot}10^{19}$
CAB18-6A	541.5	531.7	380.4	12.0	12.1	15.6	$1.6{\cdot}10^{-14}$	$1.7{\cdot}10^{-14}$	$2.1{\cdot}10^{-13}$	$1.9{\cdot}10^{20}$	$1.8{\cdot}10^{20}$	$7.1{\cdot}10^{19}$
CAB18-7A	697.1	449.5	323.7	9.9	13.8	17.6	$8.1{\cdot}10^{-15}$	$3.6{\cdot}10^{-14}$	$1.1{\cdot}10^{-13}$	$3.1{\cdot}10^{20}$	$9.6{\cdot}10^{19}$	$3.9{\cdot}10^{19}$
CAB18-12A	676.7	636.6	469.1	10.1	10.6	13.3	$1.5{\cdot}10^{-13}$	$1.8{\cdot}10^{-13}$	$4.8{\cdot}10^{-13}$	$1.7{\cdot}10^{19}$	$1.5{\cdot}10^{19}$	$7.0{\cdot}10^{18}$
CAB18-18A	641.2	580.8	436.9	10.6	11.4	14.1	$4.9{\cdot}10^{-14}$	$6.8{\cdot}10^{-14}$	$1.7{\cdot}10^{-13}$	$5.4{\cdot}10^{19}$	$4.2{\cdot}10^{19}$	$2.0{\cdot}10^{19}$
CAB19-1	622.9	446.0	340.4	10.8	13.9	17.0	$5.4{\cdot}10^{-14}$	$1.6{\cdot}10^{-13}$	$4.0{\cdot}10^{-13}$	$5.0{\cdot}10^{19}$	$2.2{\cdot}10^{19}$	$1.1{\cdot}10^{19}$
CAB20-3	517.0	429.0	320.0	12.4	14.3	17.8	$9.9{\cdot}10^{-14}$	$1.8{\cdot}10^{-13}$	$5.0{\cdot}10^{-13}$	$3.1{\cdot}10^{19}$	$1.9{\cdot}10^{19}$	$8.9{\cdot}10^{18}$

Notes: Dchord, Dmax, and Deq refer to the results of the linear intercept, maximum diameter and equivalent area diameter methods, respectively.